Chapter Two

The Microstructure of High-Strength Weld Deposits

2.1 Introduction

The microstructure of high-strength weld deposits, Fe-C-Si-Ni-Mn-Mo alloys, which have unusually high levels of substitutional alloying additions have been studied. These alloys are being developed to ensure sound, high-strength welds for the Trident Submarine programme. In this work, the welds (provided by ESAB Ltd. UK) were deposited using the manual metal welding technique. The electrodes used were of a nominal E10016-G type as defined by the American Welding Society, the joint geometry being compatible with BS 639. The welding was carried out in the flat position using the stringer bead technique, the parent plate thickness being 20mm. The welding current and voltage used were 180A and 23V (DC+) respectively (arc energy ≈ 2 KJ/mm), the weld consisting of some 21 runs with 3 runs per layer deposited at a speed of about 0.002 m/s; the interpass temperature was typically 250°C. The electrode diameter was 4mm.

By varying the composition of the 4mm diameter electrode used (but keeping the welding conditions constant throughout), weld deposits with different carbon or molybdenum concentrations were obtained; the chemical analyses are presented in Table II.1. The chemical determinations were carried out using a direct reading spectrograph. The level of oxygen and nitrogen were determined using Leco furnaces, and it was found that content of oxygen and nitrogen were about 320 and 100 ppm respectively in all the weld deposits. The mechanical properties of these weld metals except WB are listed in Table II.2.

Before investigating the microstructure of the weld metals, the calculated isothermal transformation curves and phase diagrams of the alloys are presented. In multirun welds, the volume fraction of reheated weld metal is large. Hence, besides the microstructure of fusion zone, that of the reheat zone has also been studied. Inclusions in weld metal have been regarded as an important factor in the development of microstructure; therefore, inclusions are also studied.

2.2 Calculated Isothermal Transformation Curves and Phase Diagrams

It is easier to study phase transformations and to study theoretical alloy steel design if isothermal transformation curves and phase diagrams of the specific alloy steels are available. Bhaseshia [156] has presented thermodynamic models, allowing the calculation of reaction start time for Time-Temperature-Transformation curves, and Bhadeshia and Edmonds [89,100] have also developed the theory for the calculation of phase diagrams for multicomponent steel. Hence, it is possible to compute the T_0, $T_0^{'}$ and $Ae_3^{'}$ curves which are important in understanding transformation in welds. The T_0 curve [157] is defined such that stress free austenite and ferrite of the same composition (with respect to both the interstitial and substitutional alloying elements) have equal free energy. The corresponding curve for austenite and ferrite (with a certain amount of stored energy associated with transformation strains) of identical composition and free energy is called the $T_0^{'}$ curve [89,100]. On the other hand, with paraequilibrium [32] , the no substitutional element partitioning $Ae_3^{'}$ curve [89,100] describes the equilibrium between α and γ when carbon partitioning is allowed to occur subject to the constraint that the substitutional elements do not redistribute during transformation. An application of such methods towards the prediction of the microstructure (allotriomorphic ferrite, Widmanstätten ferrite, acicular ferrite and microphases) of the fusion zone of low-alloy steel weld deposits has also been considered by Bhadeshia et al. [1]. The thermodynamic calculation presented in subsequent sections were carried out using computer programs developed by Bhadeshia and co-workers.

2.2.1 Theory for the Calculation of Isothermal Transformation Diagrams

Bhadeshia [156] has presented a method to calculate the reaction start times for the Time-Temperature-Transformation (TTT) curves for alloy steels containing C, Mn, Si, Ni, Cr, Mo, and V in any combination, as long as the total substitutional alloying addition is limited to less than about 7 wt%. Such diagrams can be treated as being composed of two C curves. The upper C curve represents the time taken for the initiation of diffusional transformation such as allotriomorphic ferrite and pearlite, whereas the lower C curve represents the time taken for the initiation of displacive transformation such as bainite and Widmanstätten ferrite.

The essence of this method is to fix experimental values to Russell's general equation [158] of incubation time. The incubation time can be expressed as:

$$\tau_s = \left\{ \frac{T}{(\Delta F_m)^p D} \right\} \tag{1}$$

where the braces imply a functional relation,

τ_s = incubation time taken to establish a steady state nucleation rate,

T = absolute temperature,

D = appropriate diffusion coefficient,

ΔF_m = free energy for nucleation, a function of alloy concentrations and temperature,

and p = a factor depending on the nature of the nucleus.

This method therefore precludes any preconceived ideas regarding the shape, the coherency or the size of the initial nucleus. These calculations generate two 'C' curves as a function of time and temperature. In the case of the lower 'C' curve the diagram is truncated at the bainite start temperature Bs (or Widmanstätten ferrite start temperature Ws) since this represents an upper thermodynamic limit beyond which neither Widmanstätten ferrite nor bainite can nucleate. The flat top of the lower C curve actually corresponds to the temperature at which the nucleation of displacive transformation first becomes possible. It should be noted that although the analysis does not allow for grain size variations, it has been pointed out [159] that such variations are relatively small as far as the initiation of transformation is concerned; in any case, unless site saturation occurs, the reaction-start times should not alter significantly with the usual range of austenite grain sizes obtained following commercial heat treatments.

2.2.2 Calculated Isothermal Transformation Curves

The resultant Time-Temperature-Transformation (TTT) curves for the weld metals studied in this investigation are shown in Figure II.1 and 2, and allow us to study theoretically the effect of alloying elements on the transformation.

Figure II.1 shows the TTT curves of the nine different weld metals studied in this work. It is found that all these weld metals possess good hardenability. Under the usual weld deposition conditions, a typical weld cooling rate [1,16] over the temperature range 800-500°C is less than $20^{\circ}Cs^{-1}$. Hence, the cooling curve cannot intersect the diffusional C curve. These weld deposits should consist of bainitic ferrite and residual austenite, the latter subsequently being retained to ambient temperature or transforming to microphases. It is interesting to investigate the microstructure of these high strength weld metals in detail to confirm this point.

It has been supposed [53,160] that molybdenum has a positive effect on the weld metal microstructure in the as-welded condition, by increasing the amount of acicular ferrite. The weld metals studied in this investigation were specially designed in order to elucidate any molybdenum effect. The content of molybdenum in these weld metals was varied from 0.01 to 0.57 wt%. Figure II.2 shows the effect of increasing molybdenum on the calculated TTT curves. It is found that the effect is not significant even for the 0.57 wt% of molybdenum containing alloy (as shown in Figure II.2d). This is because of the generally high alloy content of the welds, where manganese and nickel also exert a powerful influence.

2.2.3 Phase Diagrams for Transformation in Steels

It is known that the growth of both Widmanstätten ferrite and bainite is in evidence displacive [100]. Thermodynamically, Widmanstätten ferrite can only form with an equilibrium or paraequilibrium carbon content, so that growth is controlled at a rate depending on the diffusion of carbon in austenite; however, an atomic correspondence is maintained for substitutional atoms, in agreement with the observed shape change effects. On the other hand, the formation of bainite involves the propagation of displacive sub-units with a full carbon supersaturation, and partitioning of the carbon into the residual austenite occurs subsequent to transformation, rather than during the growth process.

To characterise microstructural development under isothermal transformation, the T'_0, T_0, and Ae'_3 curves are very important in understanding transformation mechanism. The calculations of T'_0 T_0, and Ae'_3 curves for weld metals studied in this investigation were carried out using the analysis of Bhadeshia and Edmonds [89], and are demonstrated in the next section. This analysis allows the extent of the isothermal reaction at any temperature to be established assuming either a bainite or Widmanstätten ferrite reaction, since the transformation should stop when the carbon content of the residual austenite reaches either the T'_0 or Ae'_3 phase boundary respectively [89,101].

2.2.4 Calculated T'_0, T_0, and Ae'_3 Curves

The T'_0, T_0, and Ae'_3 curves for weld metals have been calculated and are shown in Figure II.3; the corresponding TTT curves have been presented in Figure II.1. In essence, it should be noted that T'_0 and Ae'_3 curve can be used to define thermodynamically the limits of transformations, but TTT curves determine the kinetics of transformation and both have to be used in the theoretical design of alloys. For example, for low-alloy steels, all reactions are relatively rapid, and it should be difficult to quench γ at a rate fast enough to achieve significant transformation to bainite without avoiding the occurence of allotriomorphic ferrite and pearlite reactions.

The T'_0, T_0, and Ae'_3 curves vary only as a function of the substitutional alloying element content and are unaffected by the average carbon content of the alloy $\bar{X}$. For a given value of $\bar{X}$, when the T'_0 curve shifts to the right, the austenite can tolerate more carbon before bainite transformation becomes thermodynamically impossible, thus increasing the maximum permitted volume fraction of bainite (V_b) at any isothermal transformation temperature. Certainly, an increase in V_b can also be achieved by reducing $\bar{X}$, but the hardenability should be considered first as mentioned above. For the weld metals used in the present work, the T'_0 curves are not very different (Figure II.3), and all the values $\bar{X}$ are very small. It is expected to obtain high volume fraction of bainite in these weld metals.

2.3 Microstructure of High-Strength Weld Deposits

In Section 2.2, it has been known that all the weld metals studied in this investigation possess good hardenability, and in fact these weld metals are designed to obtain high-strength and high-toughness properties. The aim of this work is to identify the microstructural constituents of these weld metals. A macrograph of the typical manual metal arc weld deposit studied is presented in Figure II.4. It shows that the weld deposit WA1 contains 21 runs in total with 3 beads per layer. The volume fraction of reheated weld metal is large (about 0.3). Hence, besides the microstructure of the fusion zone, that of the reheated zone should be investigated.

Microstructure of the Fusion Zone

The columnar austenite grains of the fusion zone in the weld deposit WA1 are shown in Figure II.5. The austenite grain is very large, and can be treated as the form of a hexagonal prism. The width of austenite grain was measured by 1000 lines normal to grain boundaries on Quantimet 720 image analysing computer, and the value was 55μm. In the case of measurement by randon sections, it was 75μm. In a typical fusion zone microstructure, fairly continuous layer of allotriomorphic ferrite (α) usually outline the columnar grain boundaries of austenite. However, in this higher alloy weld metal WA1, the layers of allotriomorphic ferrite become thinner or even discontinuous. It is believed that solute segregation occurs during weld-pool solidification [8,40,70,78]. The distribution of solute element within austenite grain will in turn affect the final microstructure [78]. The γ/γ boundary is certainly a preferred site for the nucleation of allotriomorphic ferrite. Therefore, it is not just segregation that is important, but position of γ/γ boundary relative to segregation [70,78].

The primary microstructures of fusion zone in the weld deposits WA1, WA2, WB, WC1, WC2, WD1, WD2, WD3 and WD4 are presented in Figure II.6. It is noted that WC2 (Figure II.6e) and WD1 (Figure II.6f) contain 0.01 wt% of molybdenum respectively; WA1 (Figure II.6a), WA2 (Figure II.6b), WB (Figure II.6c), and WC1 (Figure II.6d) and WD2 (Figure II.6g) contain about 0.20 wt% of molybdenum respectively; WD3 (Figure II.6h) contains 0.40 wt% of molybdenum; and WD4 (Figure II.6i) contains 0.57 wt% of molybdenum. All the welds have a similar primary microstructure consisting mainly of acicular ferrite (volume fraction about 0.9), with very little allotriomorphic ferrite, Widmanstätten ferrite and microphases. The calculated TTT diagram indicates that allotriomorphic ferrite and Widmanstätten ferrite should not be present, probably forming due to the presence of chemical segregation in weld, which cools under non-equilibrium conditions. The γ/γ boundaries are expected to be in solute-depleted regions when the first phase to solidify is δ, since δ/δ boundaries (where the last solute-rich liquid solidifies) are in regions which are solute rich [78]. In the present study, solidification should begin with δ as the first phase to solidify, due to very low carbon content. According to the TTT diagrams, these weld metals should contain a high volume fraction of bainite. However, no classical bainite structure could be found in these primary structures. In order to predict the microstructure of the fusion zone in weld, the mechanism of the acicular ferrite transformation should be understood. A study of the thermodynamics of the acicular ferrite transformation will be presented in Chapter Three.

Thin foil specimens were prepared for transmission electron microscopy from a 0.25mm thick discs slit from the top layer (fusion zone) in weld deposits. The discs were thinned to 0.05mm by abrasion on silicon carbide paper and then electropolished in a twin jet electropolisher using a 5% perchloric acid, 25% glycerol and 70% ethanol mixture at ambient temperature, 45V. The microscopy was conducted on a Philips EM400T transmission electron microscope operated at 120kV.

The detailed morphology of acicular ferrite of these weld metals has been studied by transmission electron microscopy as presented in Figure II.7. Figure II.7a (taken from weld metal WA1) shows inclusions in the acicular ferrite plates, the inclusion diameters being about 0.3-0.6μm. In the upper region of this micrograph the microphases appear like lath martensite. In Figure II.7b (taken from weld metal WA2) the electron micrograph shows elongated microphase decorating the boundaries of ferrite plates. It is noted that a one-to-one correspondence between the number of active-inclusions and the number of acicular ferrite plates is not expected, because subsequent plates may nucleate sympathetically on any inclusion-nucleated plate [62]. Figure II.7c (taken from weld metal WD1) shows platelets of acicular ferrite which have apparently nucleated sympathetically on the austenite/ferrite interface. In some cases, several acicular ferrite plates can grow from one inclusion to give a star shaped cluster as shown in Figure II.7d (taken from weld metal WD2). Figure II.7e (taken from weld metal WD3) shows the acicular ferrite plates, inclusions, elongated microphases and blocky shaped microphases. The blocky microphases are martensite in which the auto-tempering has occurred and cementite has precipitated. In Figure II.7f (taken from weld metal WD4), the electron microscopy shows that due to hard impingement the non-parallel plates of acicular ferrite are arranged in an interlocking pattern, and small amounts of microphases are located among the acicular ferrite plates.

The lenticular shape of acicular ferrite is illustrated in Figure II.7 and since this morphology was always observed, it is concluded that acicular ferrite has in three dimensions a thin-plate morphology. The tips of the acicular ferrite plates are also found to be smoothly curved. These morphological observations are consistent with a displacive transformation mechanism in which the lenticular plate shape of acicular ferrite arises through the need to minimise the strain energy associated with the accompanying shape deformation. The dislocation density of acicular ferrite and the orientation between adjacent acicular ferrite will be dealt with in Chapter Six.

Microstructure of Reheated Zone

It has been supposed [161] that the microstructural development in the reheated zone of weld metal is generally similar to that in as-deposited weld metal, except that there is a progressive decrease in prior austenite grain size with decreasing peak temperature. Consequently, there is a progressive increase also in the ratio of allotriomorphic ferrite to acicular ferrite. The microstructure in the coarse-grained reheated region is expected to resemble that in as-deposited weld metal, except that, in the former, the present austenite grains are equiaxed.

Figure II.8a shows the reheated zone between the top layer and second layer of fusion zones in weld metal WD4. It contains elongated regions, rather like the original columnar γ grains, which are associated with microphases (maybe martensite, retained austenite, or degenerate pearlite). The microphases appear as tiny black islands in higher magnification optical micrographs as shown in Figures II.8b and c. The microphases are aligned as a banded pattern. The width between the bands is less than 20μm. However, the width of original columnar austenite grains in the fusion zone is about 60μm. It is clear that segregation within the original columnar grains causes this effect. Certainly, the banding regions are solute-rich, and are the last transformed structure in the reheated zone. In Figures II.8b and c, the micrographs show the microstructure of the reheated zone consists acicular ferrite, allotriomorphic ferrite and microphases. The volume fraction of acicular ferrite is much less than that in the fusion zone, but the amount of allotriomorphic ferrite and microphases are increased. Probably because the present austenite grains become smaller and the γ/γ boundary is located solute-depleted region, the effects enhance the nucleation and growth of allotriomorphic ferrite; therefore the volume fraction of acicular ferrite decreases in the reheated zone of weld metal studied. In order to elucidate this problem the detailed austenite grain structure and segregation pattern in reheated zone are needed.

Iron possibly picked up from metallic iron in foil.

Preliminary Study of Inclusion Chemistry

Inclusions in weld deposits have been regarded as an important factor in the development of microstructure. It is interesting to examine whether the inclusion size distribution and inclusion type determine the final microstructure of weld metal. At this stage, the inclusion chemistry of weld metal WB has been studied. The microanalysis was conducted in a Philips EM400T transmission electron microscope operated at 120 kV. An energy dispersive X-ray analysis facility was used for the microanalytical measurements, with the specimens held in a berylium holder tilted from the normal by 35°, which is the take-off angle. The X-ray count rate was optimised to about 1000 counts/s over a livetime of about 100s. The data were analysed using the LINK RTS 2 FLS program for thin foil microanalysis; this corrects that data for atomic number and absorption and accounts for overlapping peaks by fitting standard profiles. Even though the probe diameter used was about 3nm, beam spreading due to scattering of electrons within the thin foil gave an estimated broadened beam diameter of about 20nm.

Eleven different inclusions from the same specimen were tested. Because the inclusion size was large, the probe beam spreading did not cause any difficulties during analysis. The microanalytical data are shown in Figure II.9, from which it can be seen that as Fe content increases, the alloying content of Mn, Ti and Al decrease, and vice versa. It therefore seems likely that the inclusions in this weld metal are composed of two types of oxide - (Fe) oxides and (Mn, Ti, Al) oxides. (Fe) oxides may be FeO or Fe_2O_3, and (Mn, Ti, Al) oxides may be MnO, MnO_2, TiO, Ti_2O_3, TiO_2, or Al_2O_3. Note however, that all inclusions contain significant quantities of each element examined. As inclusions in the weld deposit WB studied are of very complicated composition, it is supposed that the inclusions are complex multiphases, and the potency of inclusions for ferrite nucleation cannot be estimated easily.

2.4 Summary

The calculated TTT curves and phase diagrams (To', To and Ae_3') for the high-strength weld metals have been presented. It has been shown that all the weld metals studied in this investigation possess good hardenability. The primary microstructures of the fusion zone of all weld deposits examined are similar, and consist mainly of acicular ferrite (volume fraction about 0.9), with very little allotriomorphic ferrite, Widmanstätten ferrite and microphases. The morphology of acicular ferrite has been examined by transmission electron microscopy. In addition to intragranular nucleation on inclusions, acicular ferrite also seems to nucleate sympathetically, giving rise to an interlocking formation of lenticular plates. The microstructure of the reheated zone is complicated, and a banded structure has been found in this zone. The banding region consists mainly of microphases, and reflects the segregation in original columnar austenite grain. It has also been shown that the ratio of allotriomorphic ferrite to acicular ferrite decreases in the reheated zone, probably due to austenite grain refinement and segregation effect. Inclusion chemistry has also been examined but it is difficult to draw any conclusions about nucleation potency because all the inclusions investigated seem to be complex multiphases.

Table II.1 Chemical composition of weld deposits. All concentrations are in weight percent except oxygen and nitrogen in ppm.

Weld	C	Si	Mn	Ni	Mo	Cr	V	S	P	Al	Ti	Nb	O(ppm)	N(ppm)
WA1	0.052	0.36	1.98	2.64	0.24	0.05	0.01	0.008	0.012	0.02	0.03	0.02	ND	ND
WA2	0.054	0.33	1.94	2.44	0.20	0.05	0.01	0.008	0.014	0.02	0.02	0.01	ND	ND
WB	0.060	0.27	1.84	2.48	0.20	0.05	0.01	0.005	0.012	0.01	0.02	0.01	399	111
WC1	0.040	0.37	1.70	2.36	0.20	0.04	0.02	0.008	0.015	0.02	0.03	0.01	317	98
WC2	0.040	0.33	1.62	2.44	0.01	0.04	0.01	0.008	0.014	0.02	0.02	0.01	320	107
WD1	0.030	0.38	1.73	2.39	0.01	0.05	0.01	0.005	0.008	0.02	0.02	0.01	347	58
WD2	0.031	0.40	1.68	2.46	0.17	0.04	0.01	0.005	0.008	0.02	0.03	0.01	333	80
WD3	0.035	0.41	1.89	2.64	0.40	0.05	0.01	0.005	0.010	0.01	0.02	0.01	347	59
WD4	0.034	0.43	1.80	2.48	0.57	0.05	0.01	0.005	0.009	0.01	0.02	0.01	396	61

ND = not detected by spectrographic examination

Table II.2 Mechanical Properties

	WA1	WA2	WC1	WC2	WD1	WD2	WD3	WD4
Yield Pt N/mm^2	849	740	705	667	668	719	ND	ND
UTS N/mm^2	859	781	766	721	709	757	763	759
Elongation %	18	18	24	22	22	22	10	6
Reduction of area %	68	68	ND	ND	ND	ND	ND	ND
Charpy impact energy J								
-20°C	111 99 105	133 129 129	ND	ND	141 168 164	139 148 134	121 149 134	103 106 106
-50°C	75 73 89	75 84 100	101 98 95	86 92 108	89 81 123	82 74 91	100 71 82	72 84 71
-60°C	ND	ND	69 62 94	67 47 61	ND	ND	ND	ND
-70°C	49 57 58	62 64 91	ND	ND	ND	ND	ND	ND
-80°C	ND	ND	ND	ND	33 44 47	33 46 38	43 48 46	51 52 46

ND = not determined.

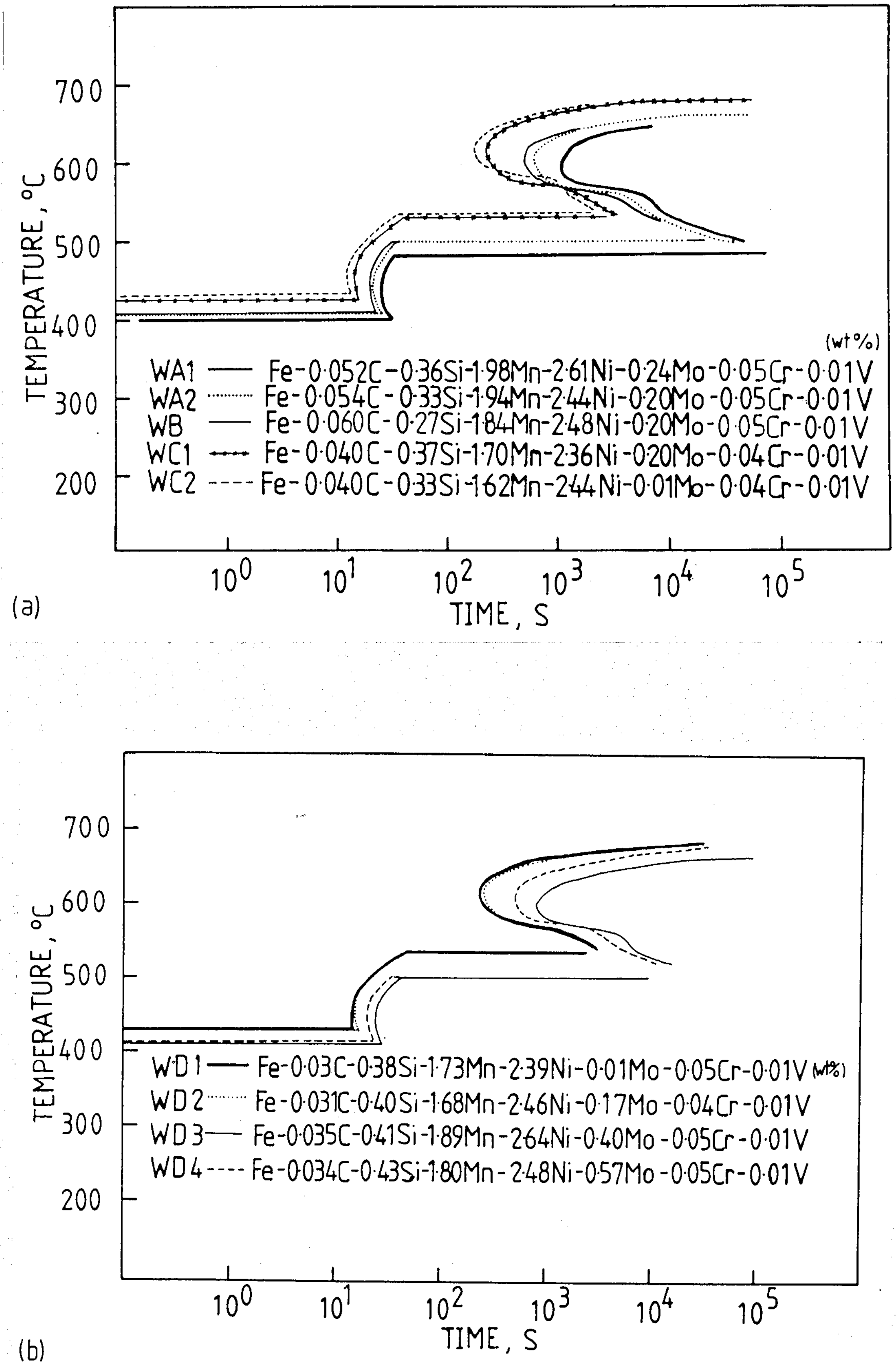

Figure II.1 - Showing the calculated TTT curves for weld metals.

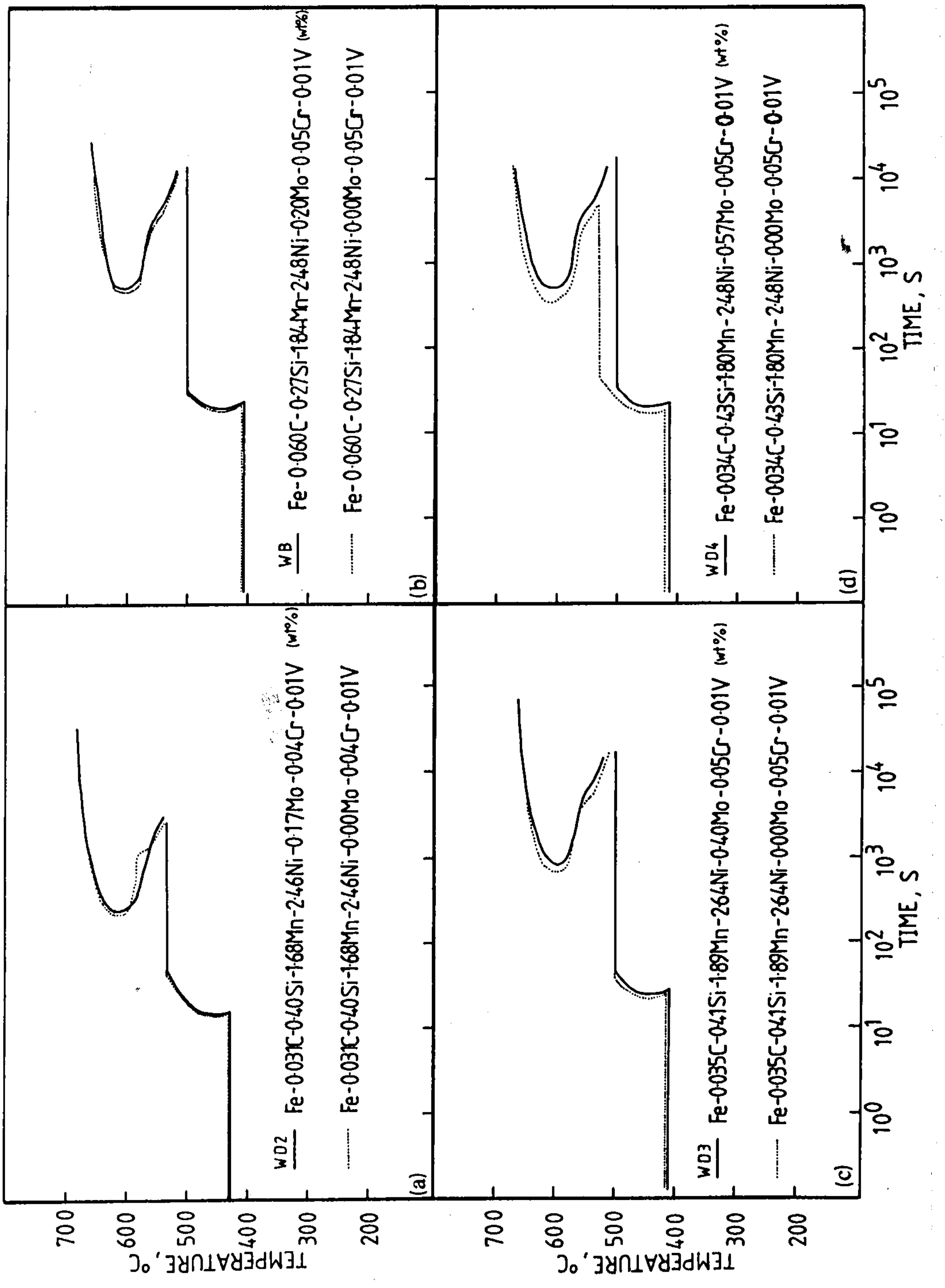

Figure II.2 - Showing the amount of molybdenum effect on the calculated TTT curves for weld metals.

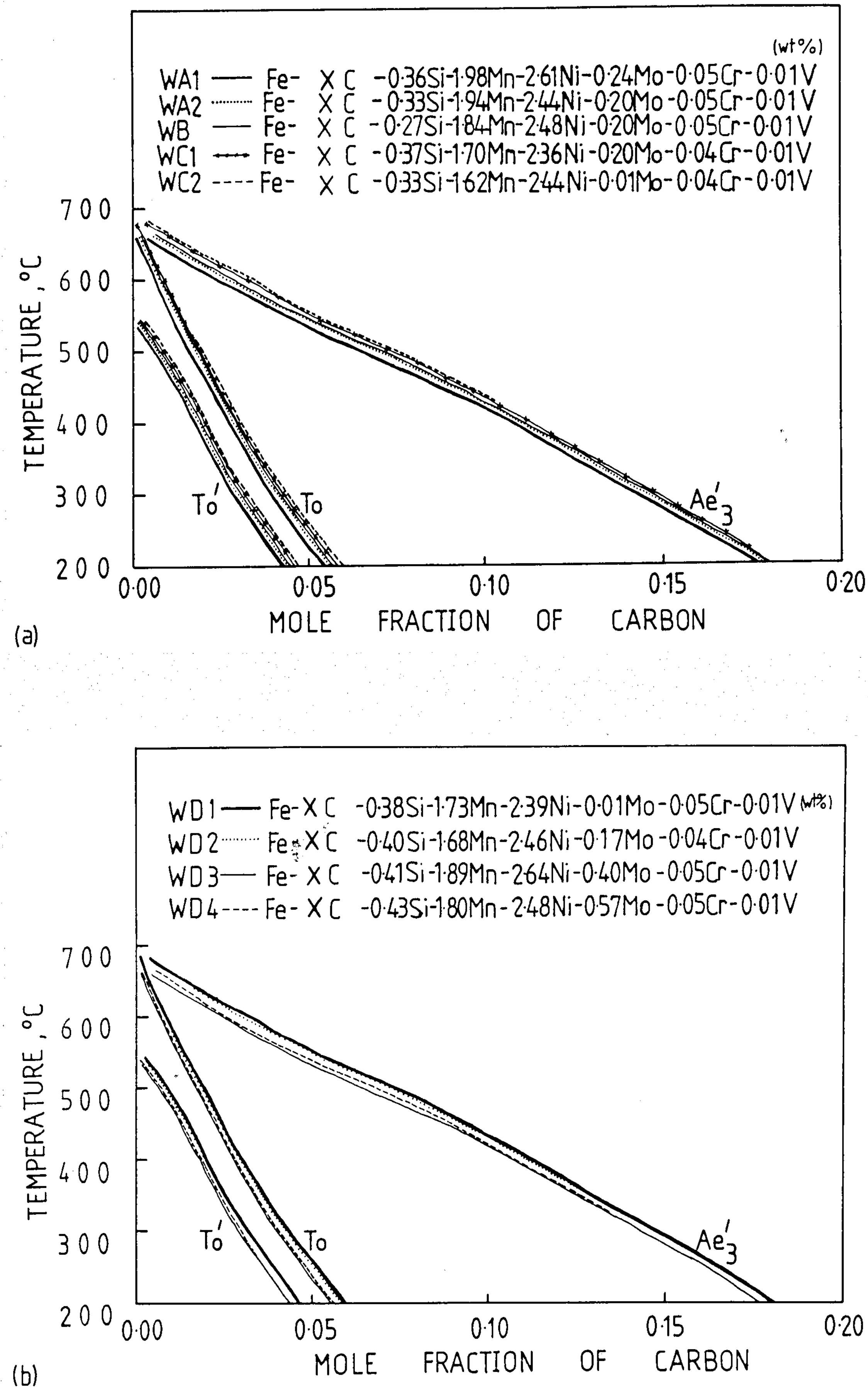

Figure II.3 - Showing the calculated T_o', T_o and Ae_3' curves for weld metals.

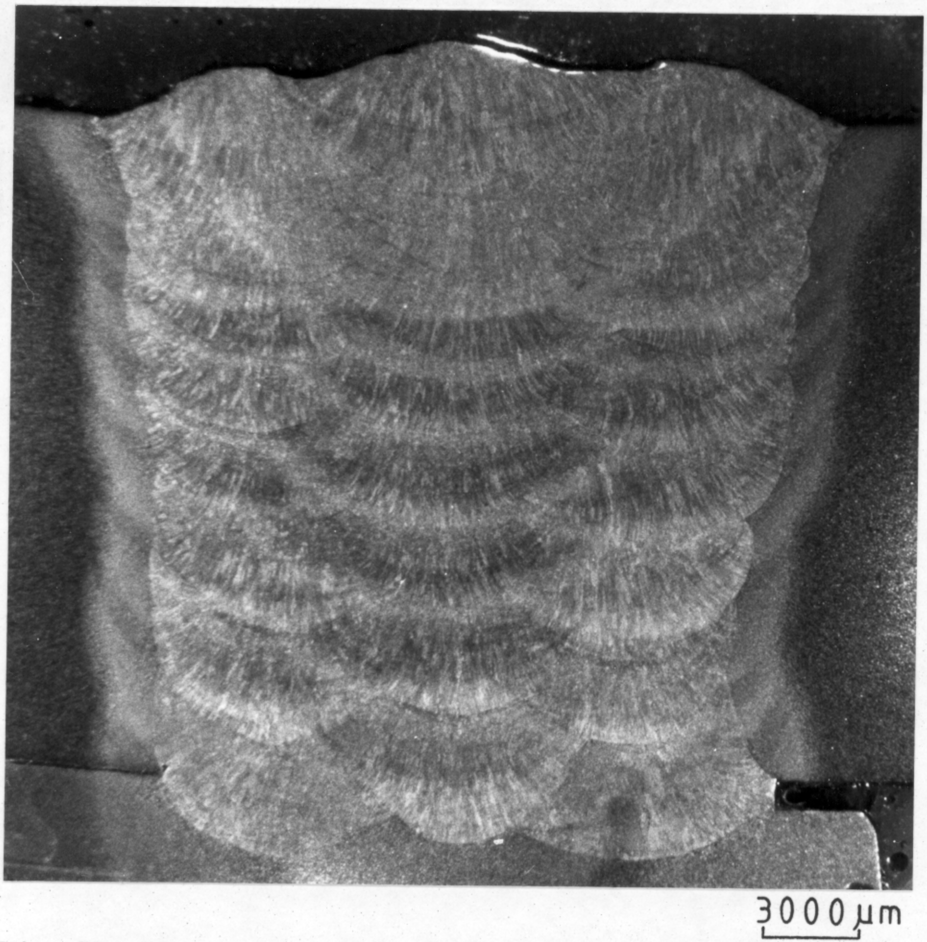

Figure II.4 - Showing the macrograph of the typical manual metal arc weld deposit studied. It contains 21 runs, and 3 beads per layer. The reheated zones can be identified.

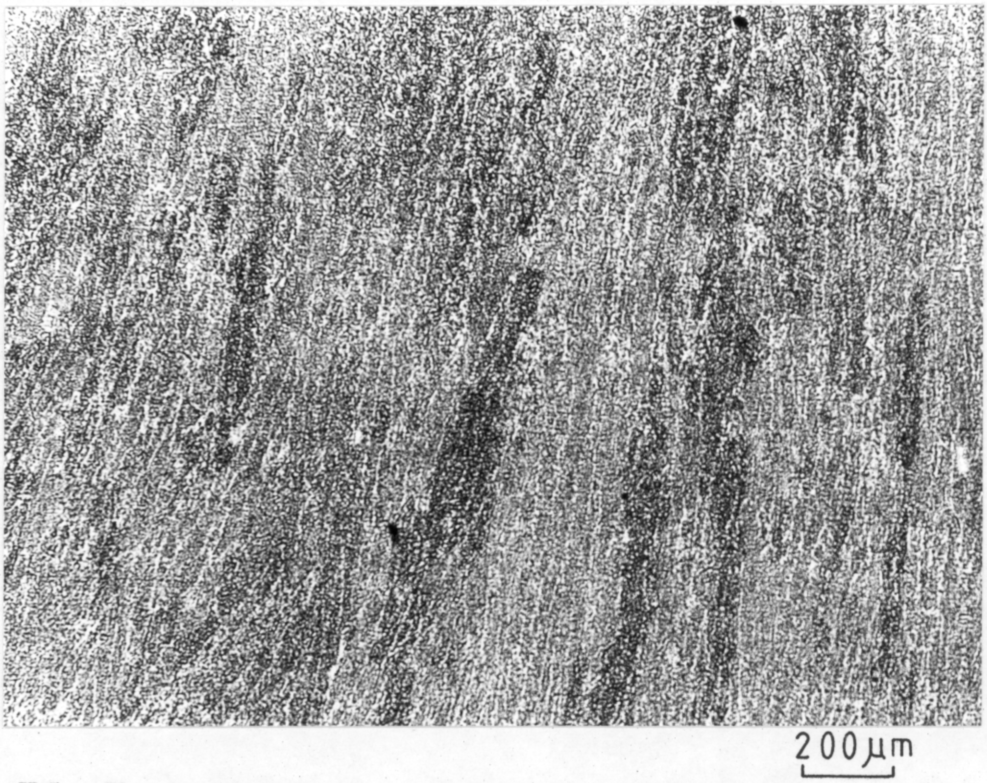

Figure.II.5 - Showing the columnar austenite grain boundaries in fusion zone of weld metal WA1.

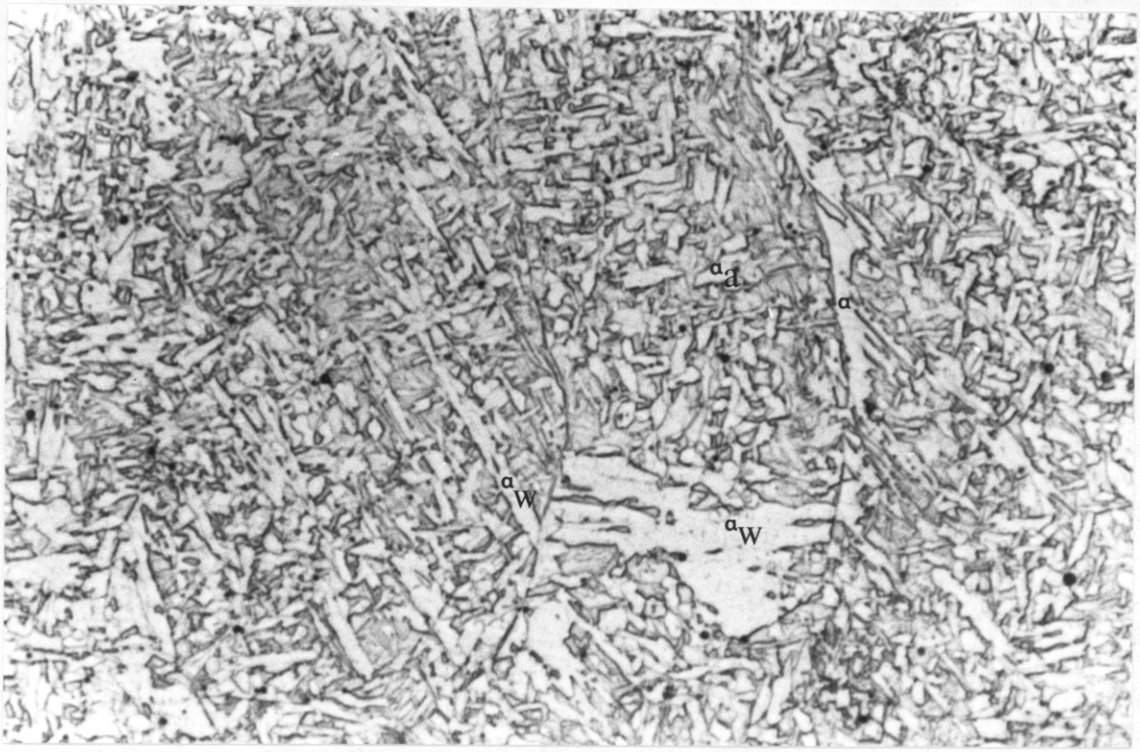

Figure II.6(a) - Primary microstructure of WA1.

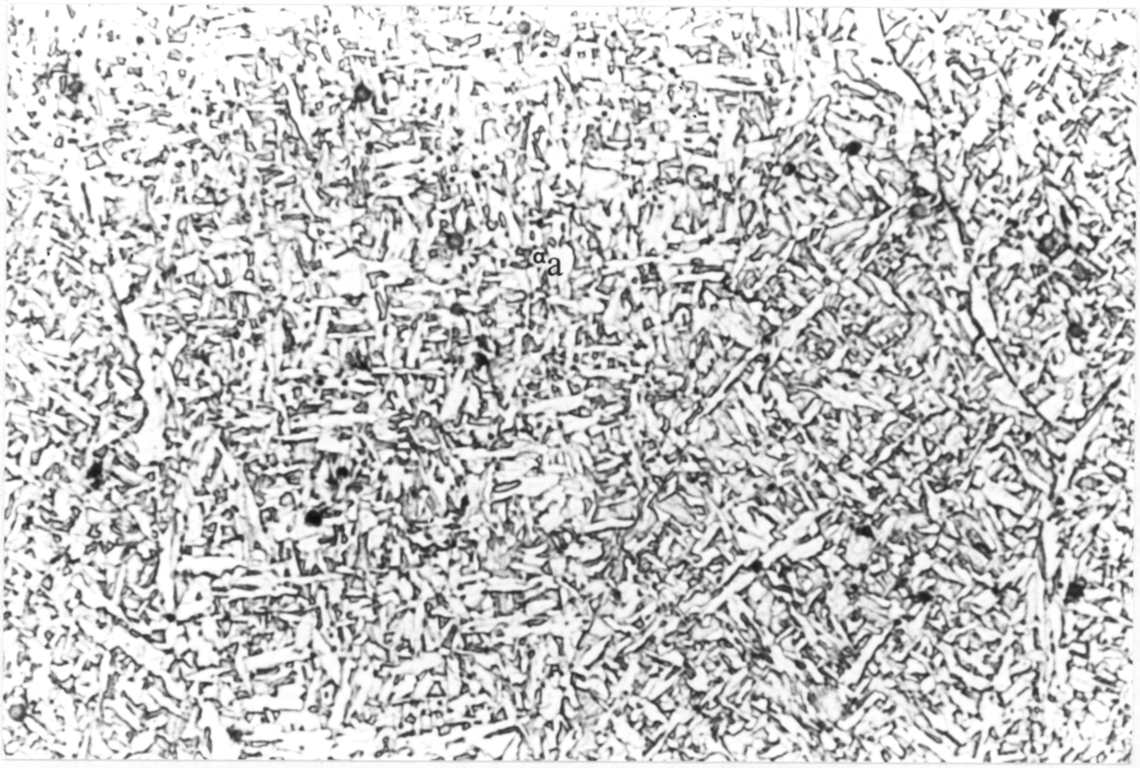

Figure II.6(b) - Primary microstructure of WA2.

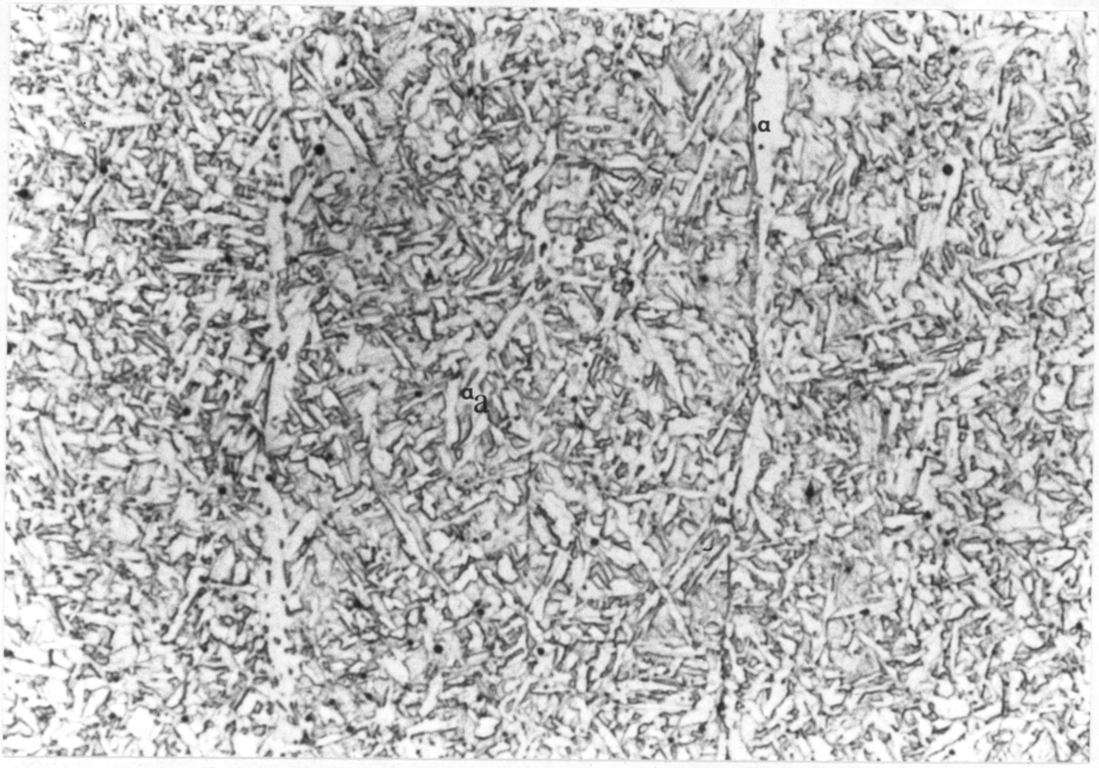

Figure II.6(c) - Primary microstructure of WB.

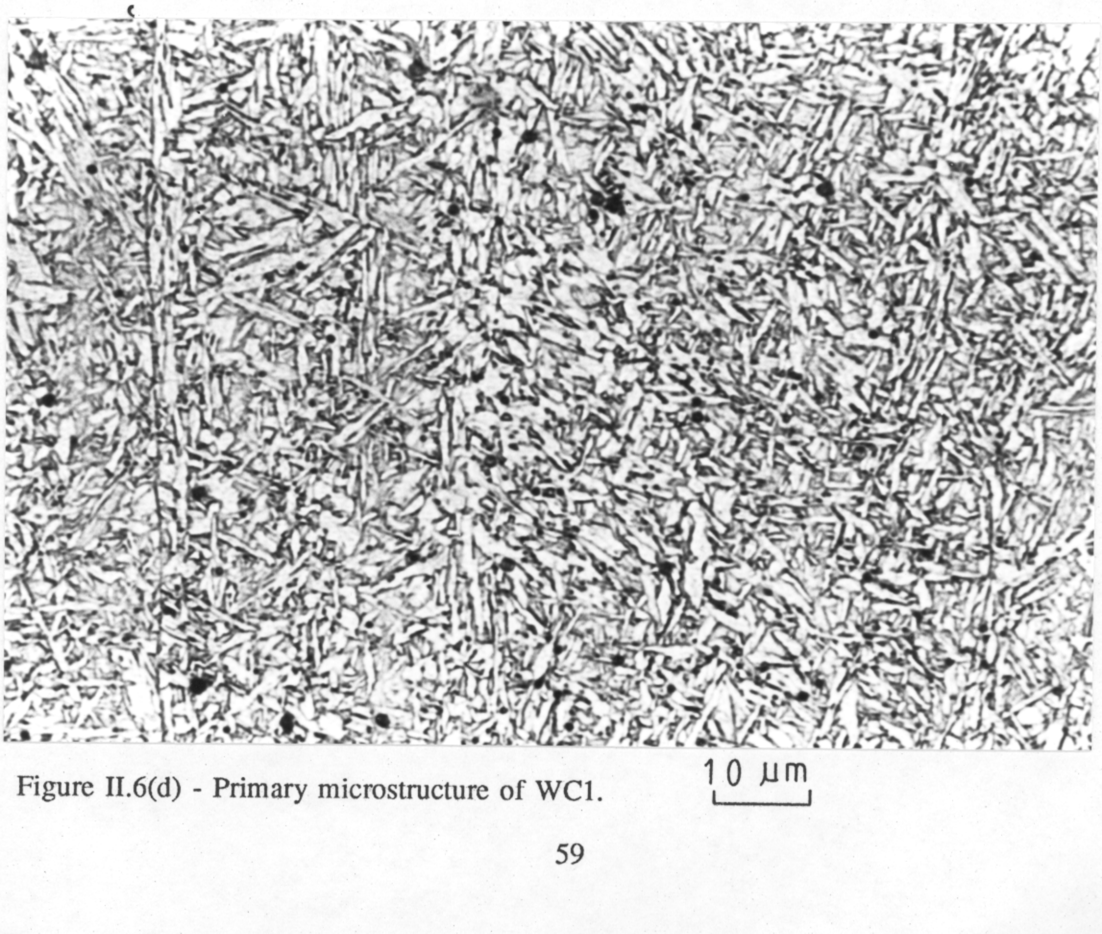

Figure II.6(d) - Primary microstructure of WC1.

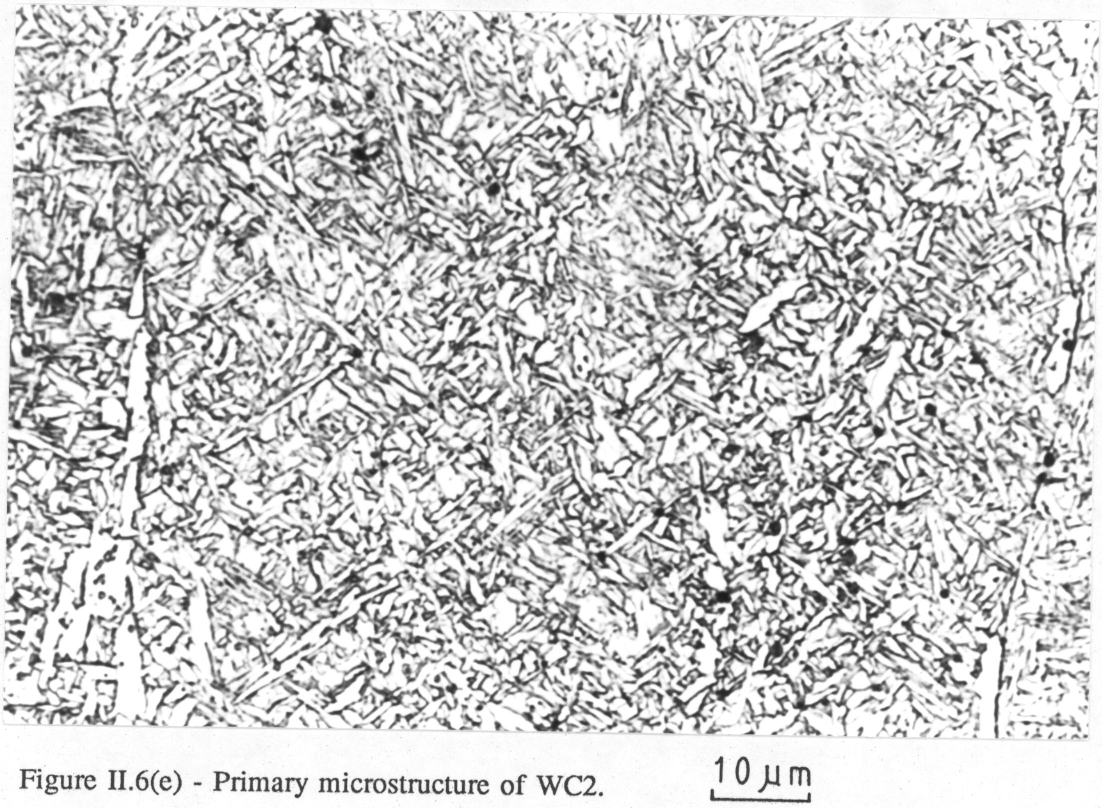

Figure II.6(e) - Primary microstructure of WC2.

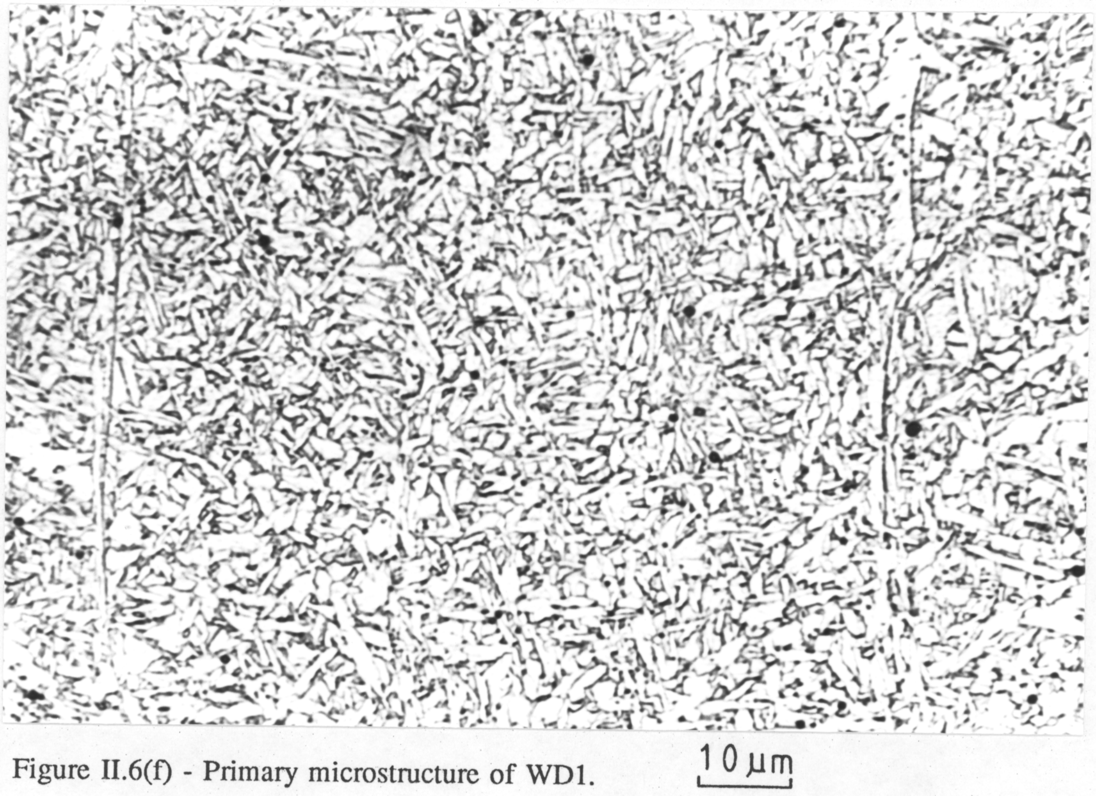

Figure II.6(f) - Primary microstructure of WD1.

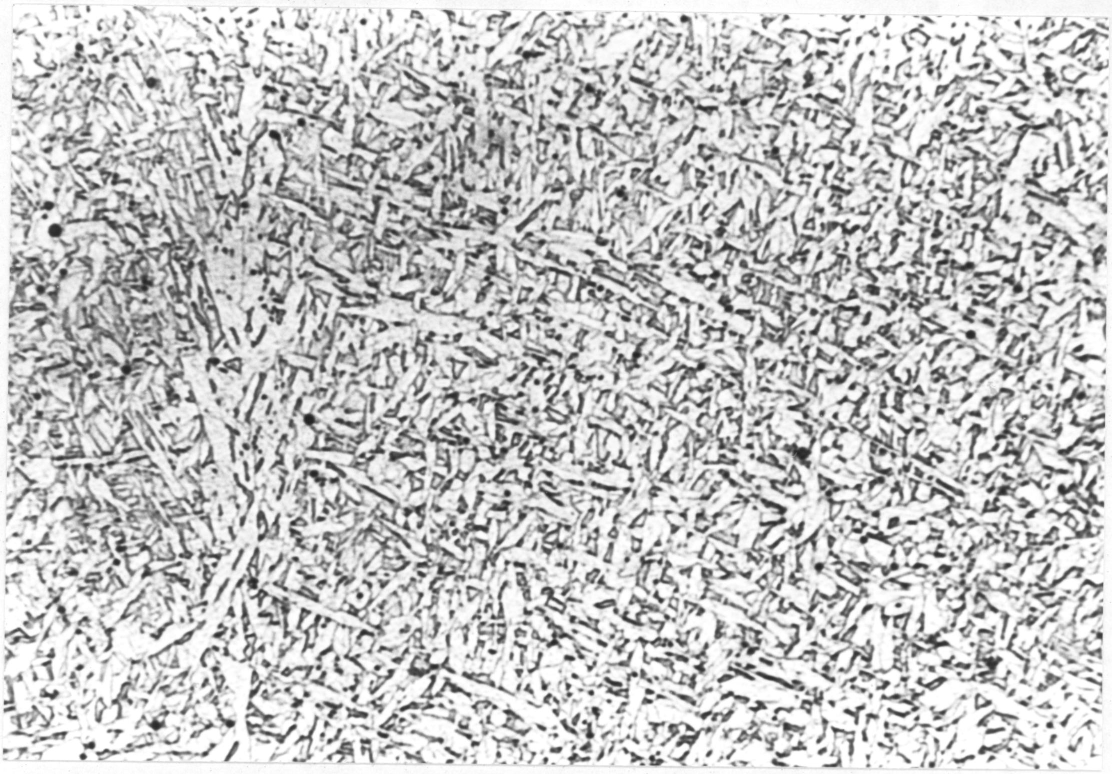

Figure II.6(g) - Primary microstructure of WD2.

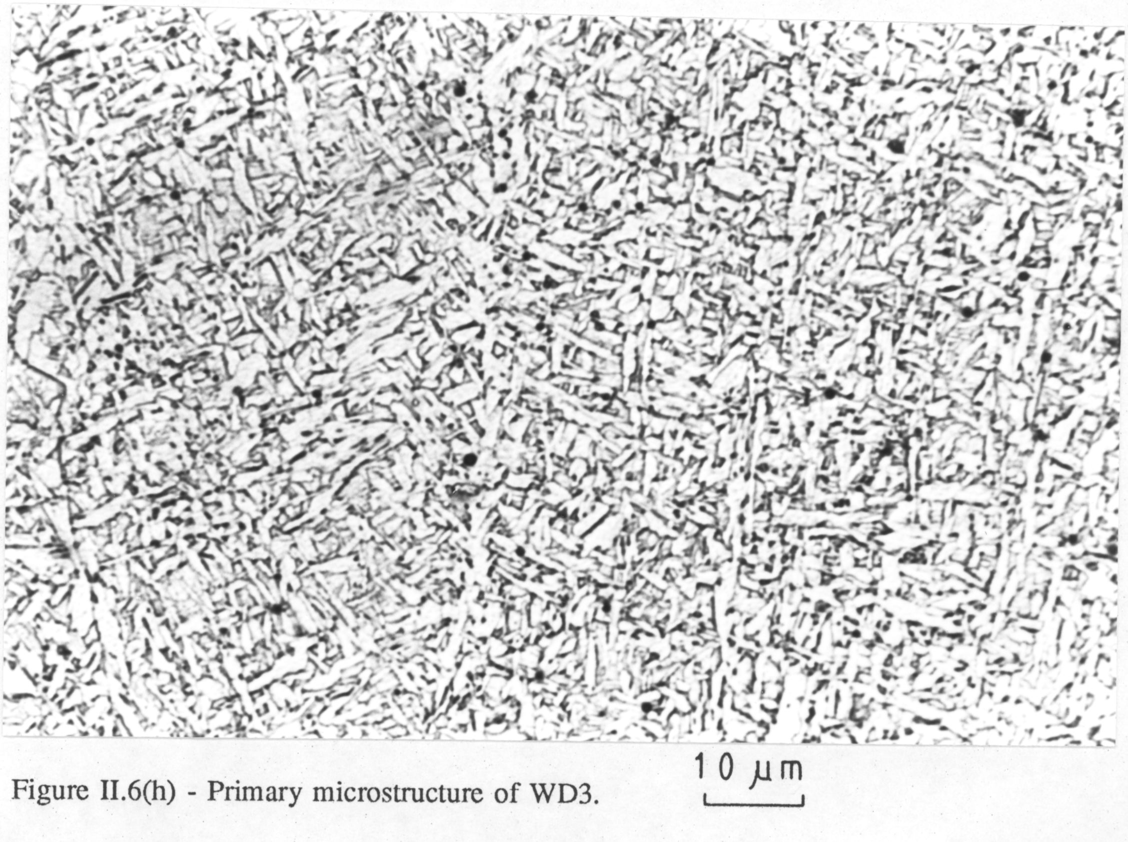

Figure II.6(h) - Primary microstructure of WD3.

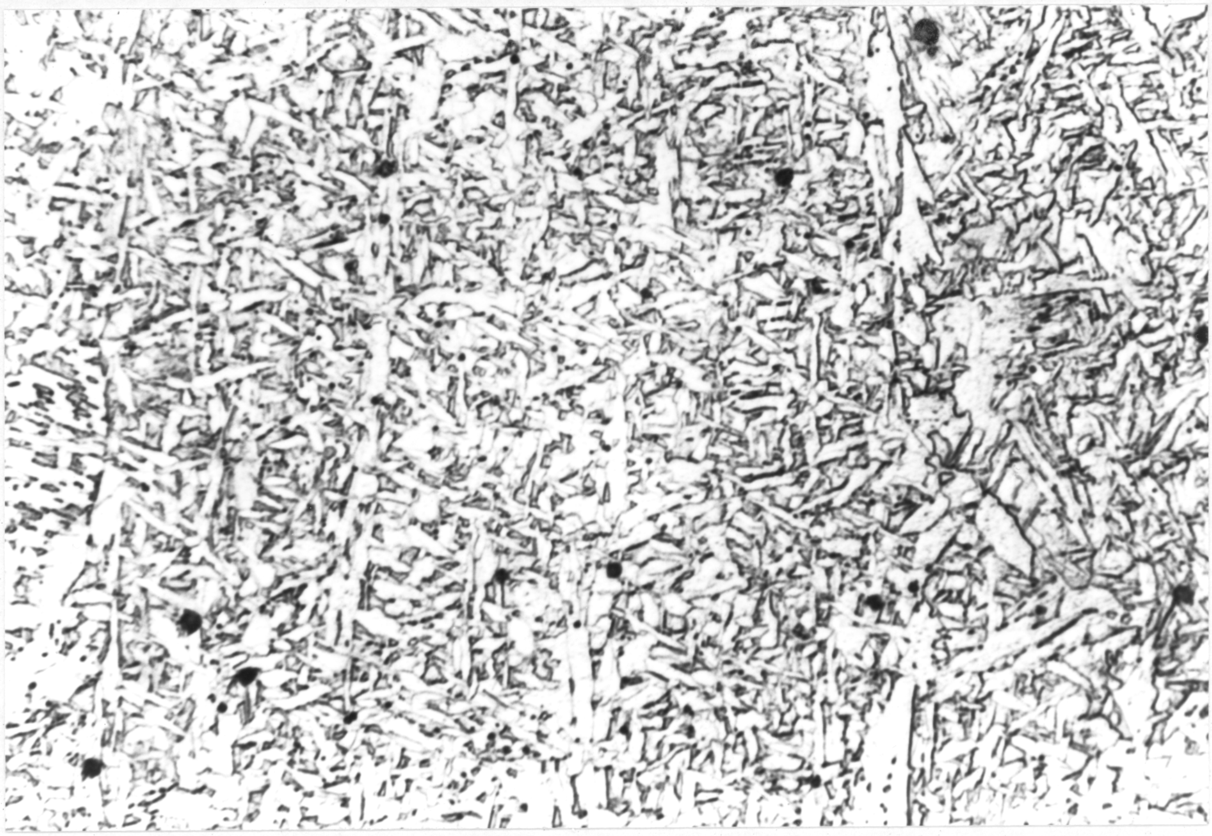

Figure II.6(i) - Primary microstructure of WD4.

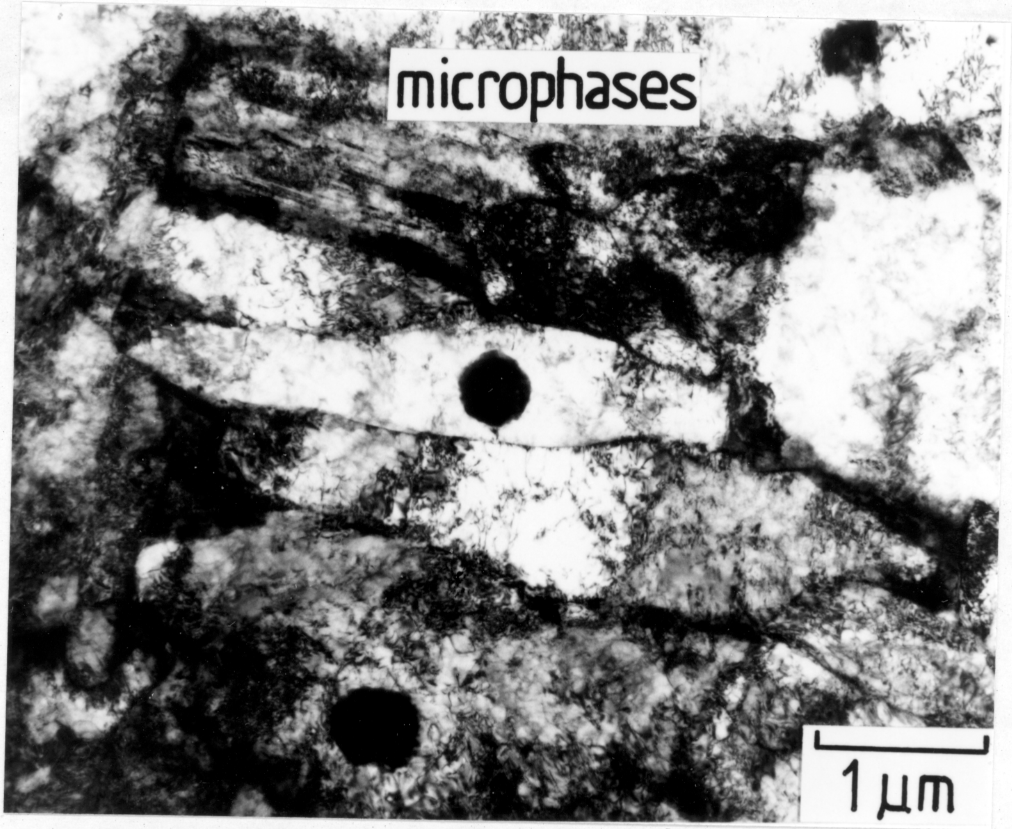

Figure II.7(a) - Electron micrograph shows the acicular ferrite, inclusions and microphases in fusion zone of weld metal WA1.

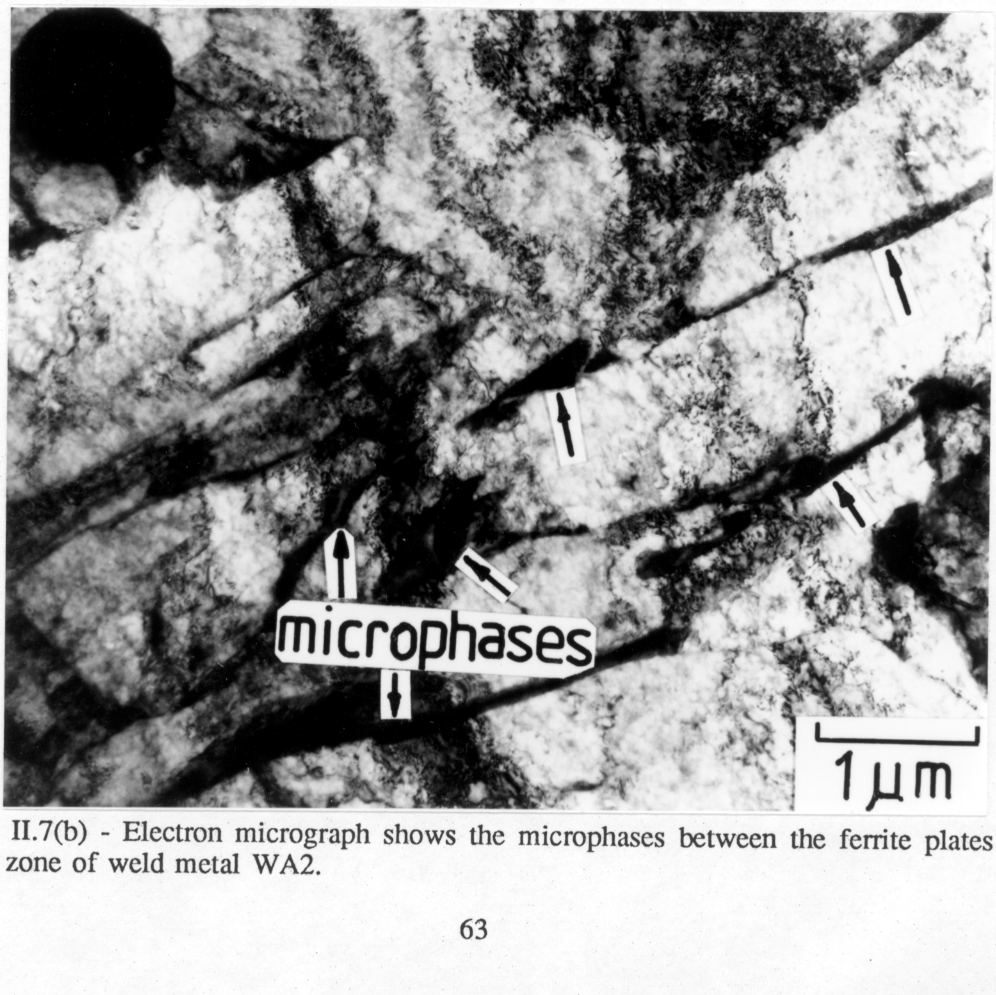

Figure II.7(b) - Electron micrograph shows the microphases between the ferrite plates in fusion zone of weld metal WA2.

Figure II.7(c) - Electron micrograph shows the acicular ferrite sympathetic nucleation in fusion zone of weld metal WD1.

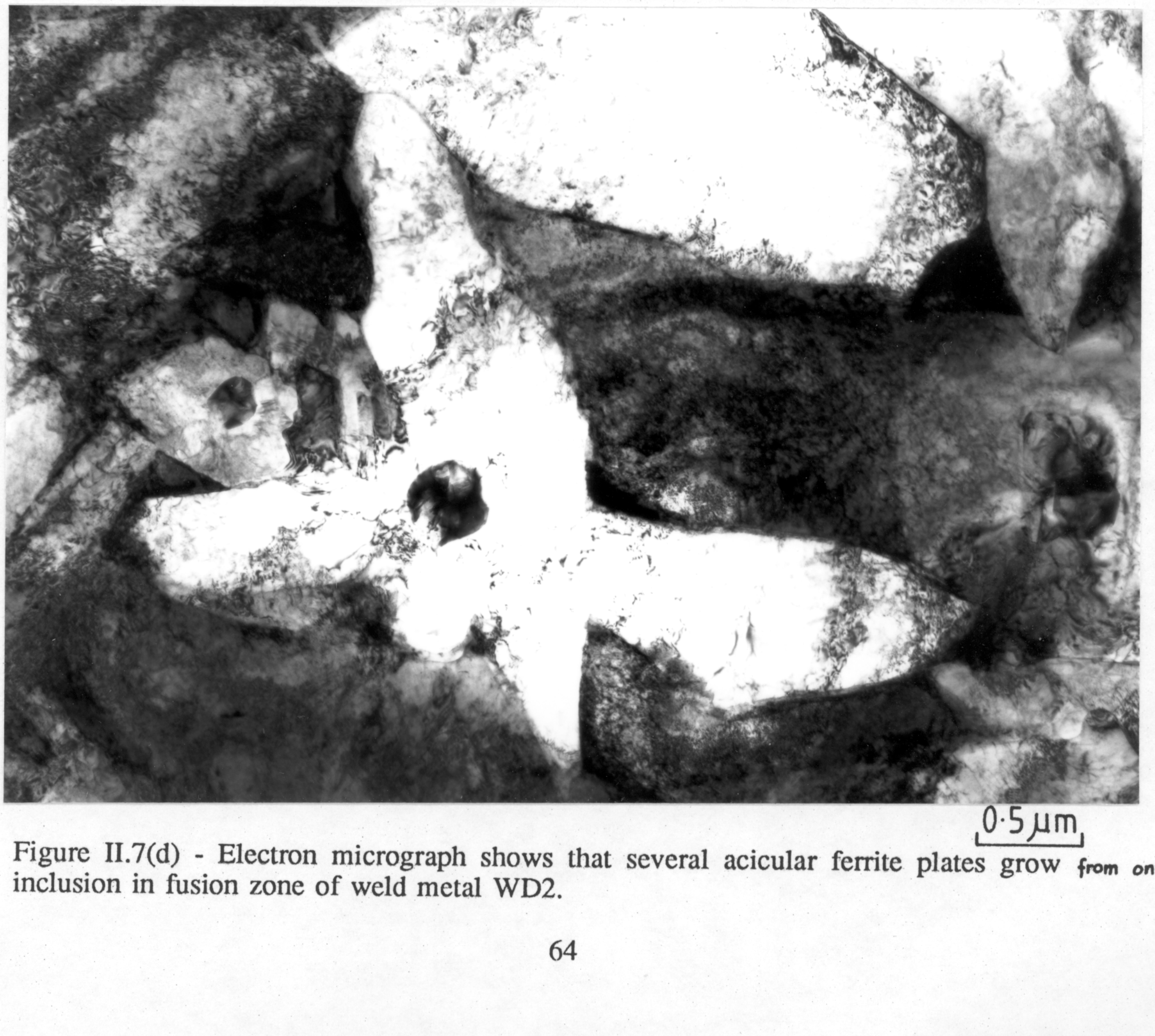

Figure II.7(d) - Electron micrograph shows that several acicular ferrite plates grow from one inclusion in fusion zone of weld metal WD2.

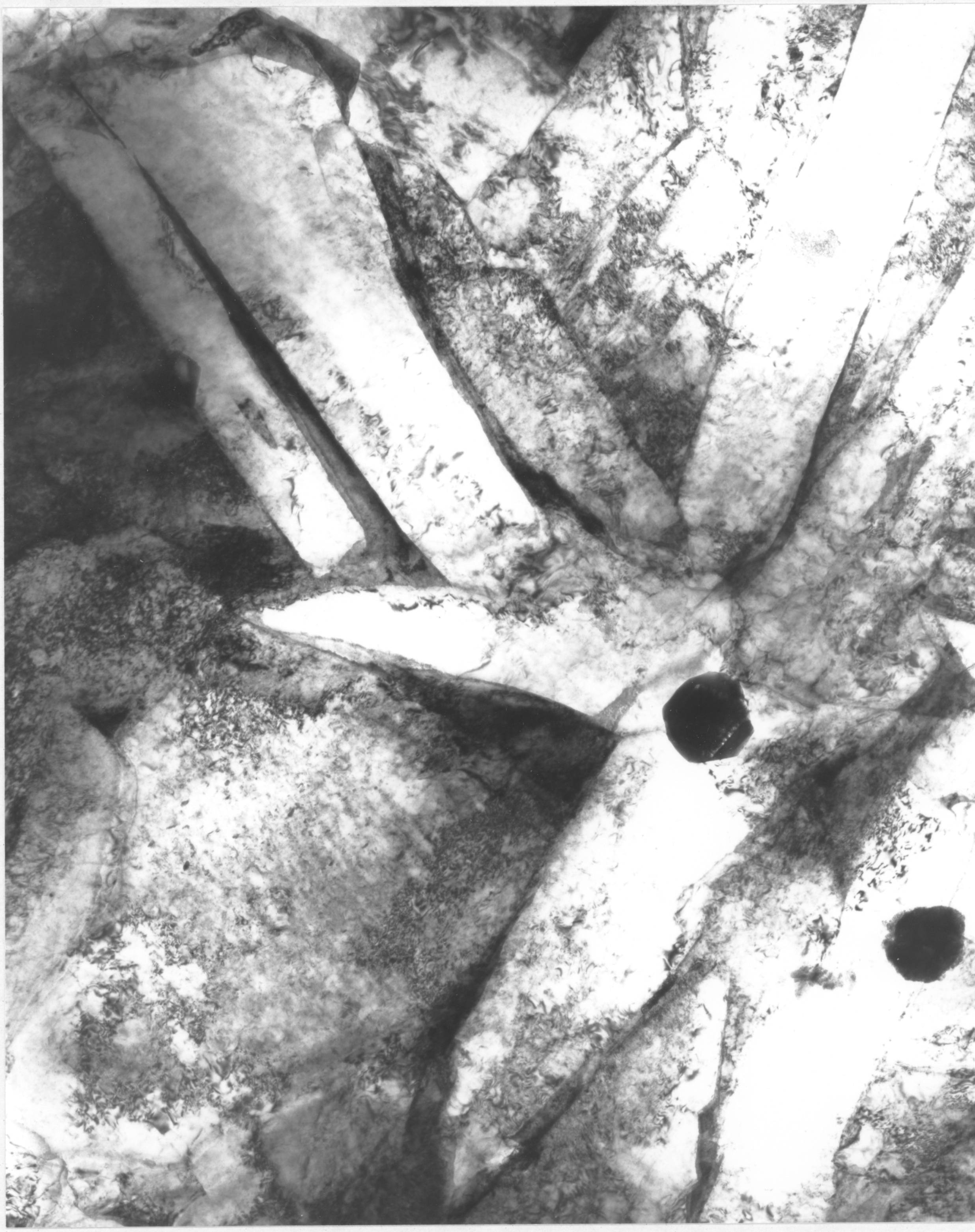

Figure II.7(e) - Electron micrograph shows the acicular ferrite plates, inclusions, elongated microphases and blocky shaped microphases in fusion zone of weld metal WD3.

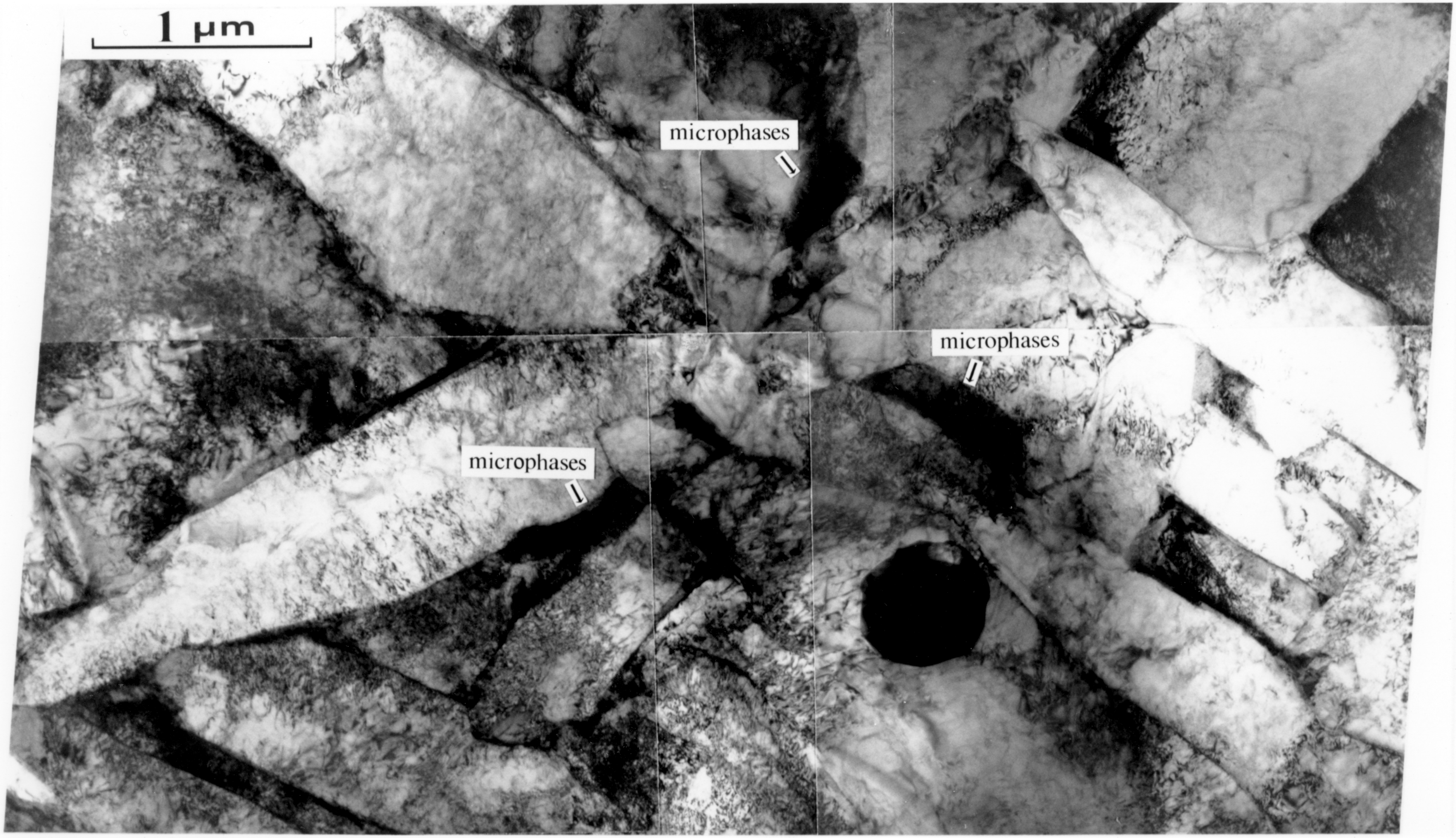

Figure II.7(f) - Electron microscopy shows that due to hard impingement the plates of acicular ferrite are arranged in an interlocking pattern in fusion zone of weld metal WD4.

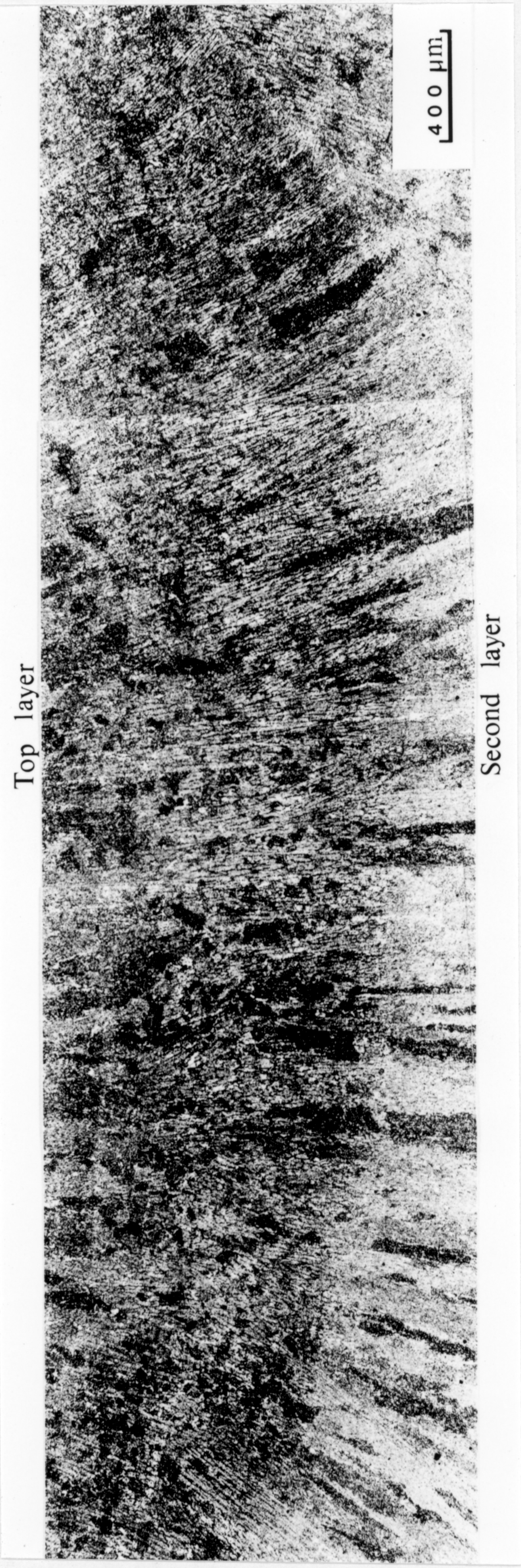

Figure II.8(a) - Showing reheated zone between the top layer and second layer of fusion zones in weld metal WD4.

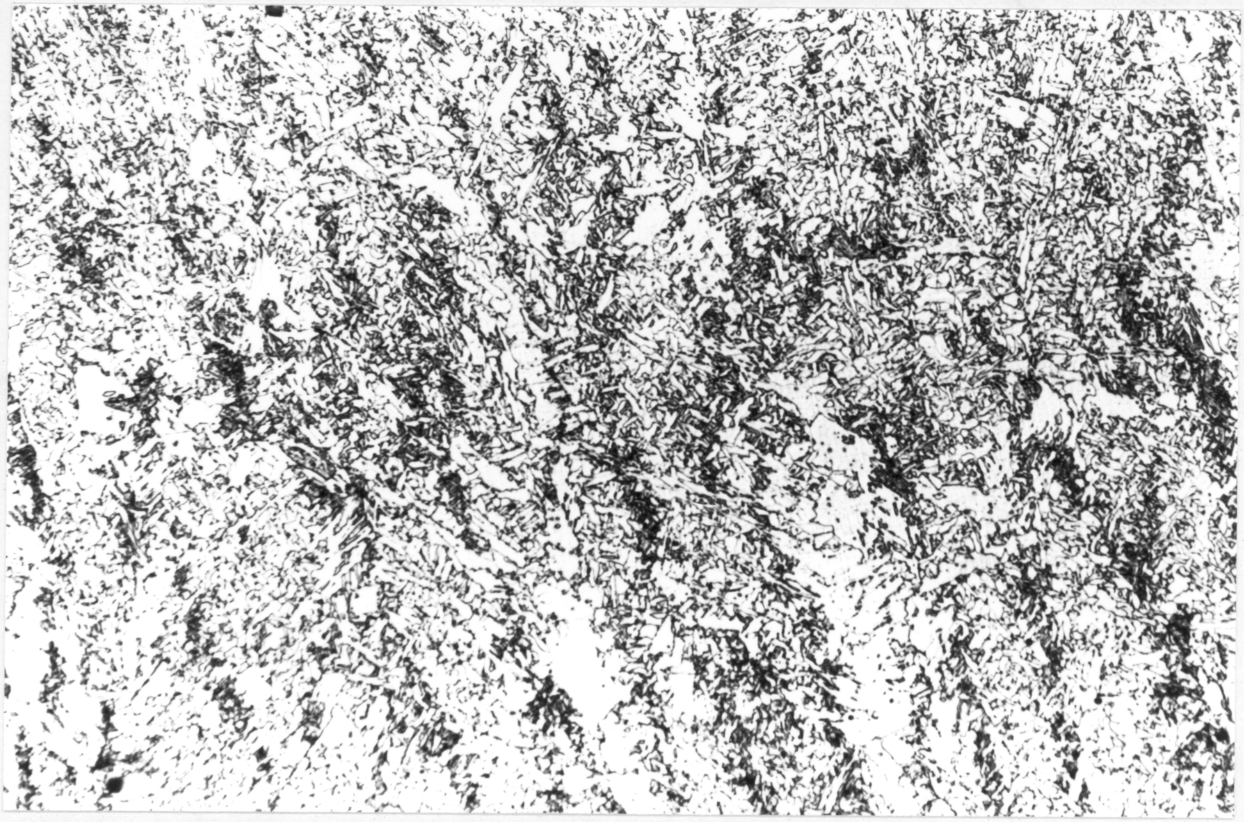

Figure II.8(b) - Showing the microstructure of reheated zone in weld metal WD4.

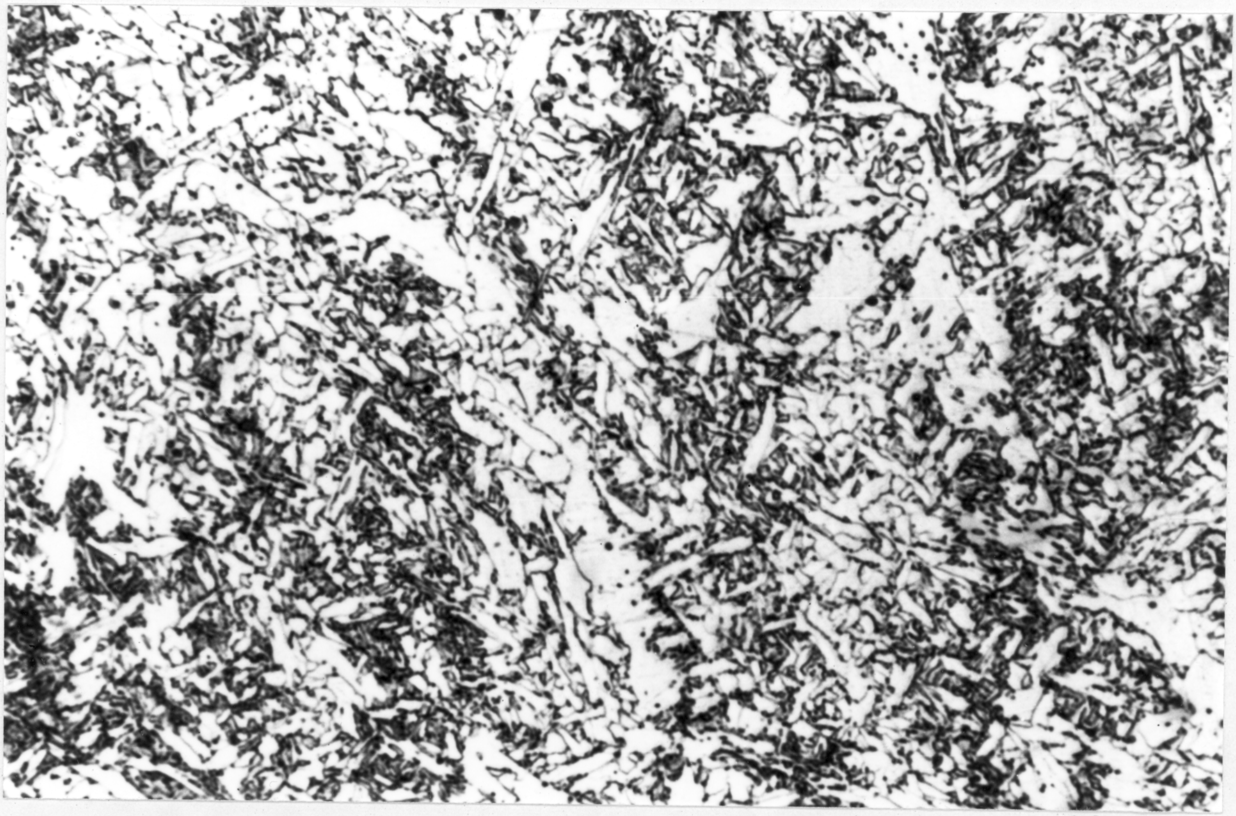

Figure II.8(c) - Showing the microstructure of reheated zone in weld metal WD4.

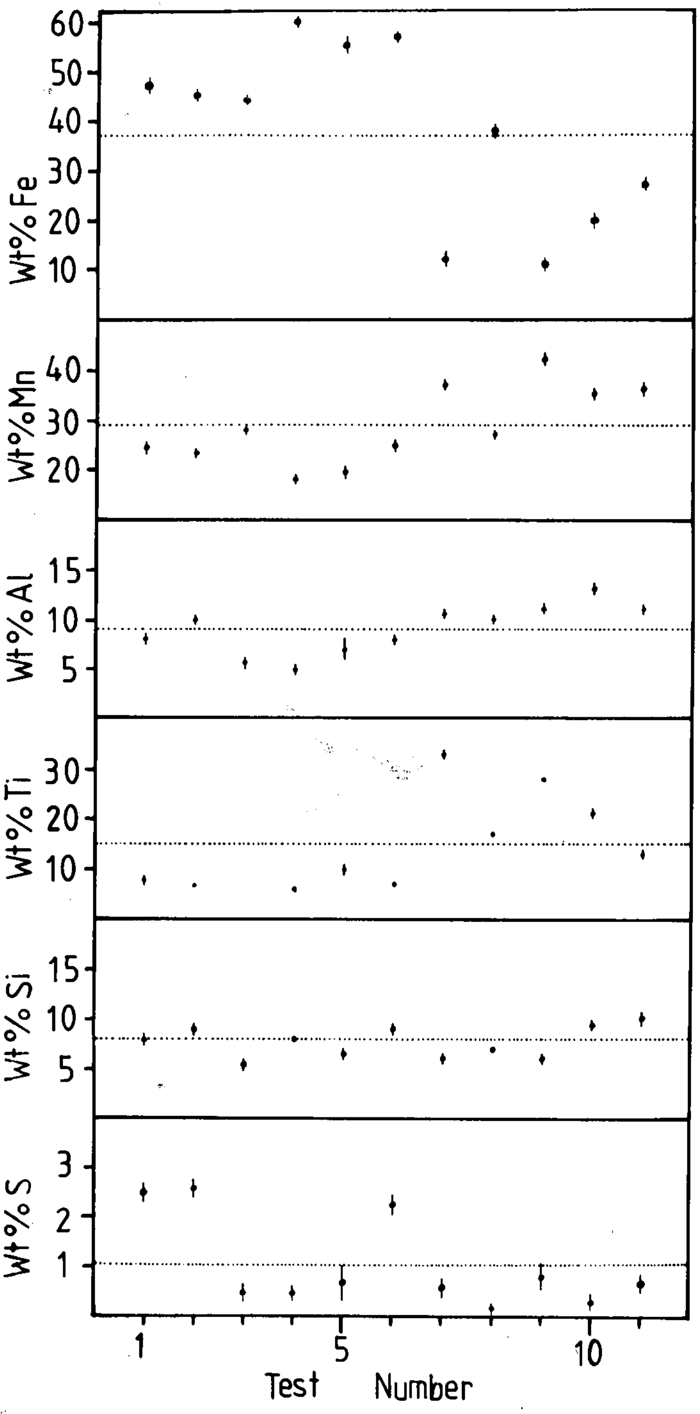

Figure II.9 - Microanalytic data on inclusions of weld metal WB